

# High-order gas-kinetic scheme with parallel computation for direct numerical simulation of turbulent flows

Guiyu Cao<sup>a</sup>, Liang Pan<sup>b,\*</sup>, Kun Xu<sup>a,c</sup>

<sup>a</sup>*Department of Mathematics, Hong Kong University of Science and Technology, Clear Water Bay, Kowloon, Hong Kong*

<sup>b</sup>*School of Mathematical Science, Beijing Normal University, Beijing, China*

<sup>c</sup>*Shenzhen Research Institute, Hong Kong University of Science and Technology, Shenzhen, China*

---

## Abstract

The performance of high-order gas-kinetic scheme (HGKS) has been investigated for the direct numerical simulation (DNS) of isotropic compressible turbulence up to the supersonic regime [9]. Due to the multi-scale nature and coupled temporal-spatial evolution process, HGKS provides a valid tool for the numerical simulation of compressible turbulent flow. Based on the domain decomposition and message passing interface (MPI), a parallel HGKS code is developed for large-scale computation in this paper. The standard tests from the nearly incompressible flow to the supersonic one, including Taylor-Green vortex problem, turbulent channel flow and isotropic compressible turbulence, are presented to validate the parallel scalability, efficiency, accuracy and robustness of parallel implementation. The performance of HGKS for the nearly incompressible turbulence is comparable with the high-order finite difference scheme, including the resolution of flow structure and efficiency of computation. Based on the accuracy of the numerical solution, the numerical dissipation of the scheme in the turbulence simulation is quantitatively evaluated. As a mesoscopic method, HGKS performs better than both lattice Boltzmann method (LBM) and discrete unified gas-kinetic scheme (DUGKS), due to its high-order accuracy. Meanwhile, based on the kinetic formulation HGKS shows advantage for supersonic turbulent flow simulation with its accuracy and robustness. The current work demonstrates the capability of HGKS as a powerful DNS tool from the low speed to supersonic turbulence study, which is less reported under the framework of finite volume scheme.

*Keywords:* High-order gas-kinetic scheme, direct numerical simulation of turbulence, parallel computation.

---

## 1. Introduction

Turbulence is ubiquitous in natural phenomena and engineering fluid applications [1, 2]. The understanding and prediction of multiscale turbulent flow is one of the most difficult

---

\*Corresponding author

*Email addresses:* gcaaaa@connect.ust.hk (Guiyu Cao), panliang@bnu.edu.cn (Liang Pan), makxu@ust.hk (Kun Xu)

problems in both mathematics and physical sciences. Direct numerical simulation (DNS) solves the Navier-Stokes equations directly, resolve all scales of the turbulent motion (above Kolmogorov scale), and eliminate modeling entirely [3, 5]. With the advances of numerical methods and super computers, great success has been achieved by DNS to accurately compute the unsteady turbulent flow, such as DNS of turbulent channel flow up to  $Re_\tau \approx 5200$  [4]. For the incompressible turbulence simulation, the spectral and pseudo-spectral method [5, 6], and lattice Boltzmann method (LBM) [7, 8] have been established and validated successfully. However, for the compressible flow simulation with discontinuous shocks [9], both of them fail to capture shocklets and suffer from numerical instability. For the compressible turbulence flow [10, 11], the high-order finite difference WENO scheme [12, 13, 14] and the high-order compact method [15] have been widely utilized. Aiming at capturing shocklets robustly and resolving smooth region accurately, the hybrid scheme combining the compact scheme and WENO scheme has been developed [16]. However, due to the numerical instability when encountering strong shocklets, the highest turbulent Mach number for hybrid scheme is still limited and critical threshold of simulating supersonic flow remains. Although the second-order finite volume scheme is the main workhorse in practical engineering applications, the DNS is reported rarely within the finite volume framework due to its over-dissipative nature [17]. Because of the advantage of the finite volume formulation, such as the excellent conservative properties and favorable ability in capturing discontinuities, it is reasonable to develop high-order finite volume scheme for direct simulation of turbulent flow in all flow regimes from subsonic to supersonic ones.

In the past decades, the gas-kinetic scheme (GKS) has been developed systematically based on the Bhatnagar-Gross-Krook (BGK) model [18, 19] under the finite volume framework, and applied successfully for the computations from low speed flow to hypersonic one [20, 21]. Different from the classical methods with Riemann solvers [22], the gas-kinetic scheme presents a gas evolution process from kinetic scale to hydrodynamic scale, where both inviscid and viscous fluxes are recovered from a time-dependent and genuinely multi-dimensional gas distribution function at a cell interface. In discontinuous shock region, the kinetic scale particle transport physics takes effect to construct a crisp and stable shock transition. In smooth flow region, the accurate Navier-Stokes solution can be obtained once the flow structure is well resolved. Starting from a time-dependent flux function, based on the two-stage fourth-order formulation [23, 24], a high-order gas-kinetic scheme has been constructed and applied for the compressible flow simulation [25, 26, 27]. The fourth-order and even higher-order can be achieved in GKS with the implementation of the traditional second-order or third-order GKS evolution model. More importantly, the high-order GKS is as robust as the second-order scheme and works perfectly from the subsonic to hypersonic viscous heat conducting flows [28]. In recent years, the gas-kinetic scheme has been applied in the turbulent flow simulation successfully as well. For high-Reynolds number turbulent flow, the gas-kinetic scheme coupled with traditional eddy viscosity turbulence model has been developed and implemented in turbulent flow study [29, 30, 31].

Recently, with the implementation of two-stage temporal discretization and WENO reconstruction, high-order gas-kinetic scheme (HGKS) in three dimensional space has been successfully developed in the DNS for isotropic compressible turbulence [9], which is the

first attempt by gas-kinetic scheme to the DNS study. The isotropic compressible turbulence with high turbulent Mach number up to supersonic regime has been studied, which verifies the validity of HGKS for compressible turbulence study, especially in the high speed regime. In order to resolve the small-scale flow structure and present the results at high Reynolds number, the development of a parallel HGKS is necessary. Here, the domain decomposition and message passing interface (MPI) [32] will be implemented in HGKS. Then, the classical turbulent tests from nearly incompressible flow to the hypersonic one, including Taylor-Green vortex, turbulent channel flow, and isotropic compressible turbulence, are used to validate the parallel scalability, efficiency, accuracy, and robustness of HGKS. The performance of HGKS is compared with the classical methods, including the popular high-order finite difference scheme [33], lattice Boltzmann method (LBM), and discrete unified gas-kinetic scheme (DUGKS) [34]. For the nearly incompressible flows, the performance of HGKS is comparable with the finite difference scheme, including the resolution and efficiency of computation. As a mesoscopic method, HGKS performs better than both LBM and DUGKS. Meanwhile, HGKS shows advantage for supersonic turbulence study due to its accuracy and robustness. For the isotropic compressible turbulence, the cases with high turbulent Mach number can be simulated without any special treatment. The current study provides us confidence on the further investigation of compressible turbulence, such as shock-boundary interaction and supersonic turbulent boundary layer transition.

This paper is organized as follows. In Section 2, the high-order gas-kinetic scheme and the strategy of parallelization are introduced. Section 3 includes numerical simulation and discussions. The last section is the conclusion.

## 2. High-order GKS and parallel implementation

### 2.1. High-order GKS

The three-dimensional BGK equation [18, 19] can be written as

$$f_t + uf_x + vf_y + wf_z = \frac{g - f}{\tau}, \quad (1)$$

where  $\mathbf{u} = (u, v, w)$  is the particle velocity,  $f$  is the gas distribution function,  $g$  is the three-dimensional Maxwellian distribution and  $\tau$  is the collision time. The collision term satisfies the compatibility condition

$$\int \frac{g - f}{\tau} \psi d\Xi = 0, \quad (2)$$

where  $\psi = (1, u, v, w, \frac{1}{2}(u^2 + v^2 + w^2 + \xi^2))^T$ ,  $\xi^2 = \xi_1^2 + \dots + \xi_N^2$ ,  $d\Xi = dudvdwd\xi_1 d\xi_N$ ,  $\gamma$  is the specific heat ratio and  $N = (5 - 3\gamma)/(\gamma - 1)$  is the internal degree of freedom.

Taking moments of the BGK equation Eq.(1) and integrating with respect to space, the finite volume scheme can be expressed as

$$\frac{d(Q_{ijk})}{dt} = \mathcal{L}(Q_{ijk}), \quad (3)$$

where the operator  $\mathcal{L}$  is defined as

$$\mathcal{L}(Q_{ijk}) = -\frac{1}{|\Omega_{ijk}|} \sum_{p=1}^6 \mathbb{F}_p(t), \quad (4)$$

where  $\Omega_{ijk} = \bar{x}_i \times \bar{y}_j \times \bar{z}_k$  with  $\bar{x}_i = [x_i - \Delta x/2, x_i + \Delta x/2]$ ,  $\bar{y}_j = [y_j - \Delta y/2, y_j + \Delta y/2]$ ,  $\bar{z}_k = [z_k - \Delta z/2, z_k + \Delta z/2]$ ,  $\mathbb{F}_p(t)$  is the numerical flux across the cell interface  $\Sigma_p$ . The numerical flux in  $x$ -direction is given as example

$$\mathbb{F}_p(t) = \iint_{\Sigma_p} F(Q) \cdot \mathbf{n} d\sigma = \sum_{m,n=1}^2 \omega_{mn} \int \psi u f(\mathbf{x}_{i+1/2,j_m,k_n}, t, \mathbf{u}, \xi) d\Xi \Delta y \Delta z,$$

where  $\mathbf{n}$  is the outer normal direction. In this paper, the orthogonal Cartesian mesh is considered, the normal direction is constant for each cell interface. The Gaussian quadrature is used over the cell interface, where  $\omega_{mn}$  is the quadrature weight,  $\mathbf{x}_{i+1/2,m,n} = (x_{i+1/2}, y_{j_m}, z_{k_n})$  and  $(y_{j_m}, z_{k_n})$  is the Gauss quadrature point of cell interface  $\bar{y}_j \times \bar{z}_k$ . The gas distribution function  $f(\mathbf{x}_{i+1/2,j_m,k_n}, t, \mathbf{u}, \xi)$  in the local coordinate can be given by the integral solution of BGK equation Eq.(1) as follows

$$f(\mathbf{x}_{i+1/2,j_m,k_n}, t, \mathbf{u}, \xi) = \frac{1}{\tau} \int_0^t g(\mathbf{x}', t', \mathbf{u}, \varsigma) e^{-(t-t')/\tau} dt' + e^{-t/\tau} f_0(-\mathbf{u}t, \xi),$$

where  $\mathbf{u} = (u, v, w)$  is the particle velocity,  $\mathbf{x}' = \mathbf{x}_{i+1/2,j_m,k_n} - \mathbf{u}(t - t')$  is the trajectory of particles,  $f_0$  is the initial gas distribution function, and  $g$  is the corresponding equilibrium state. With the first order spatial derivatives, the second-order gas distribution function at cell interface can be expressed as

$$\begin{aligned} f(\mathbf{x}_{i+1/2,j_m,k_n}, t, \mathbf{u}, \xi) = & (1 - e^{-t/\tau})g_0 + ((t + \tau)e^{-t/\tau} - \tau)(\bar{a}_1 u + \bar{a}_2 v + \bar{a}_3 w)g_0 \\ & + (t - \tau + \tau e^{-t/\tau})\bar{A}g_0 \\ & + e^{-t/\tau}g_r[1 - (\tau + t)(a_1^r u + a_2^r v + a_3^r w) - \tau A^r]H(u) \\ & + e^{-t/\tau}g_l[1 - (\tau + t)(a_1^l u + a_2^l v + a_3^l w) - \tau A^l](1 - H(u)), \quad (5) \end{aligned}$$

where the equilibrium state  $g_0$  and the corresponding conservative variables  $Q_0$  can be determined by the compatibility condition

$$\int \psi g_0 d\Xi = Q_0 = \int_{u>0} \psi g_l d\Xi + \int_{u<0} \psi g_r d\Xi.$$

With the reconstruction of macroscopic variables, the coefficients in Eq.(5) can be fully

determined by the reconstructed derivatives and compatibility condition

$$\begin{aligned}\langle a_1^k \rangle &= \frac{\partial Q_k}{\partial x}, \langle a_2^k \rangle = \frac{\partial Q_k}{\partial y}, \langle a_3^k \rangle = \frac{\partial Q_k}{\partial z}, \langle a_1^k u + a_2^k v + a_3^k w + A^k \rangle = 0, \\ \langle \bar{a}_1 \rangle &= \frac{\partial Q_0}{\partial x}, \langle \bar{a}_2 \rangle = \frac{\partial Q_0}{\partial y}, \langle \bar{a}_3 \rangle = \frac{\partial Q_0}{\partial z}, \langle \bar{a}_1 u + \bar{a}_2 v + \bar{a}_3 w + \bar{A} \rangle = 0,\end{aligned}$$

where  $k = l, r$  and  $\langle \dots \rangle$  are the moments of the equilibrium  $g$  and defined by

$$\langle \dots \rangle = \int g(\dots) \psi d\Xi.$$

More details of the gas-kinetic scheme can be found in the literatures [20, 21, 35]. Thus, the gas distribution function is determined, and the numerical flux can be obtained by taking moments of it. For the high-order spatial accuracy, the fifth-order WENO method [13, 14] is adopted. For the three-dimensional computation, the dimension-by-dimension reconstruction is used. More details about spatial reconstruction can be found in previous work [25, 9], and several remarks are given.

**Remark 1.** *For the low speed flows, such as Taylor-Green vortex problem and turbulent channel flow, the flow fields are smooth without strong shocklets, the simplified smooth second-order gas-kinetic flux [27] and WENO scheme with linear weights are used to avoid the numerical dissipation from artificially created interface discontinuity. For the tangential reconstruction  $Q_{l,r}$  and  $Q_0$ , the fourth-order polynomials are constructed at the horizontal and vertical direction. The variables and spatial derivatives can be constructed at the Gaussian quadrature points. For the compressible isotropic turbulence from subsonic to supersonic regime, the WENO-Z [14] scheme is used. In order to eliminate the spurious oscillation and improve the stability, the reconstruction can be performed for the characteristic variables in local coordinate for each Gaussian quadrature point. The characteristic variable is defined as  $\omega = R^{-1}Q$ , where  $Q$  is variable in the local coordinate, and where  $R$  is the right eigenmatrix of Jacobian matrix  $(\partial F / \partial Q)_G$  at Gaussian quadrature point. With the reconstructed variable, the conservative variables can be obtained by the inverse projection. For the tangential reconstruction of  $Q_{l,r}$  and  $Q_0$ , the variables at the ends of cell interface can be obtained from the fifth-order WENO method at the horizontal and vertical direction. With reconstructed variables and the cell averaged variables, the quadratic polynomials can be constructed. The variables and spatial derivatives can be constructed at the Gaussian quadrature points as well.*

Based on the time-dependent flux function of the generalized Riemann problem solver (GRP) [23, 24] and gas-kinetic scheme, a two-stage fourth-order time-accurate discretization was developed for Lax-Wendroff type flow solvers [25, 26]. Consider the following time dependent equation

$$\frac{\partial Q}{\partial t} = \mathcal{L}(Q),$$

with the initial condition at  $t_n$ , i.e.,

$$Q(t = t_n) = Q^n,$$

where  $\mathcal{L}$  is an operator for spatial derivative of flux, the state  $Q^{n+1}$  at  $t_{n+1} = t_n + \Delta t$  can be updated with the following formula

$$\begin{aligned} Q^* &= Q^n + \frac{1}{2}\Delta t\mathcal{L}(Q^n) + \frac{1}{8}\Delta t^2\partial_t\mathcal{L}(Q^n), \\ Q^{n+1} &= Q^n + \Delta t\mathcal{L}(Q^n) + \frac{1}{6}\Delta t^2(\partial_t\mathcal{L}(Q^n) + 2\partial_t\mathcal{L}(Q^*)). \end{aligned} \quad (6)$$

It can be proved that for hyperbolic equations the above temporal discretization provides a fourth-order time accurate solution for  $Q^{n+1}$ . To implement two-stage fourth-order method for Eq.(3), a linear function is used to approximate the time dependent numerical flux

$$\mathbb{F}_p(t) \approx \mathbb{F}_p^n + \partial_t\mathbb{F}_p^n(t - t_n). \quad (7)$$

Integrating Eq.(7) over  $[t_n, t_n + \Delta t/2]$  and  $[t_n, t_n + \Delta t]$ , we have the following two equations

$$\begin{aligned} \mathbb{F}_p^n\Delta t + \frac{1}{2}\partial_t\mathbb{F}_p^n\Delta t^2 &= \int_{t_n}^{t_n+\Delta t} \mathbb{F}_p(t)dt, \\ \frac{1}{2}\mathbb{F}_p^n\Delta t + \frac{1}{8}\partial_t\mathbb{F}_p^n\Delta t^2 &= \int_{t_n}^{t_n+\Delta t/2} \mathbb{F}_p(t)dt. \end{aligned}$$

The coefficients  $\mathbb{F}_p^n$  and  $\partial_t\mathbb{F}_p^n$  at the initial stage can be determined by solving the linear system. According to Eq.(4),  $\mathcal{L}(Q_i^n)$  and the temporal derivative  $\partial_t\mathcal{L}(Q_i^n)$  at  $t^n$  can be constructed by

$$\mathcal{L}(Q_i^n) = -\frac{1}{|\Omega_i|} \sum_{p=1}^6 \mathbb{F}_p^n, \quad \partial_t\mathcal{L}(Q_i^n) = -\frac{1}{|\Omega_i|} \sum_{p=1}^6 \partial_t\mathbb{F}_p^n.$$

The flow variables  $Q^*$  at the intermediate stage can be updated. Similarly,  $\mathcal{L}(Q_i^*), \partial_t\mathcal{L}(Q_i^*)$  at the intermediate state can be constructed and  $Q^{n+1}$  can be updated as well.

## 2.2. Parallel implementation

Due to the explicit formulation of HGKS, a popular parallel strategy is developed, where two-dimensional domain decomposition is used. As shown in Fig.1, the total number of cells is  $N_x \times N_y \times N_z$ , and the computational domain is divided into  $n_y$  parts in  $y$ -direction,  $n_z$  parts in  $z$ -direction and no division is used in  $x$ -direction. The processor  $P_{jk}, j = 0, \dots, n_y - 1, k = 0, \dots, n_z - 1$  handles a sub-domain with  $N_x \times n_{y_j} \times n_{z_k}$  cells, where

$$\begin{cases} n_{y_j} = [N_y/n_y] + 1, & j < \text{mod}(N_y, n_y), \\ n_{y_j} = [N_y/n_y], & j \geq \text{mod}(N_y, n_y), \end{cases}$$

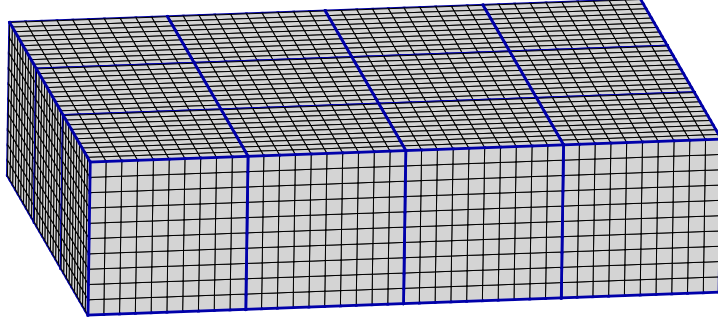


Figure 1: Schematic for two-dimensional domain decomposition with  $n_y = 4, n_z = 3$ .

and

$$\begin{cases} nz_k = [N_z/n_z] + 1, & k < \text{mod}(N_z, n_z), \\ nz_k = [N_z/n_z], & k \geq \text{mod}(N_z, n_z). \end{cases}$$

The data communication is performed between eight neighboring sub-domains, and the specific boundary conditions are performed for the boundary processor. The procedure is the only data communication of the algorithm, which is handled by the MPI libraries [32].

### 3. Numerical simulation and discussion

In this section, numerical tests from the nearly incompressible flow to the supersonic one will be presented to validate our numerical scheme. For the smooth flow without discontinuities, the collision time takes

$$\tau = \frac{\mu}{p}.$$

For the flow with discontinuities, we have

$$\tau = \frac{\mu}{p} + C \left| \frac{p_l - p_r}{p_l + p_r} \right| \Delta t,$$

where  $p_l$  and  $p_r$  denote the pressure on the left and right sides of the cell interface,  $\mu$  is the dynamic viscous coefficient,  $C = 1$  and  $p$  is the pressure at the cell interface. The reason for including artificial dissipation through the additional term in the particle collision time is to enlarge the kinetic scale physics in the discontinuous region for the construction of a numerical shock structure through the particle free transport and inadequate particle collision in order to keep the non-equilibrium property.

#### 3.1. Taylor-Green vortex

Taylor-Green vortex is a classical problem in fluid dynamics developed to study vortex dynamics, turbulent transition, turbulent decay and energy dissipation process [36, 37]. It is

given by a simple construction, and contains several key physical processes including vortex stretching, interaction and dilatation effects. Therefore, this case becomes an excellent case for the evaluation of turbulent flow simulation methodologies, and has been used by many authors for high-order method validation [33, 38]. The flow is computed within a periodic square box defined as  $-\pi L \leq x, y, z \leq \pi L$ . With a uniform temperature, the initial condition is given by

$$\begin{aligned} U &= V_0 \sin\left(\frac{x}{L}\right) \cos\left(\frac{y}{L}\right) \cos\left(\frac{z}{L}\right), \\ V &= -V_0 \cos\left(\frac{x}{L}\right) \sin\left(\frac{y}{L}\right) \cos\left(\frac{z}{L}\right), \\ W &= 0, \\ p &= p_0 + \frac{\rho_0 V_0^2}{16} \left( \cos\left(\frac{2x}{L}\right) + \cos\left(\frac{2y}{L}\right) \right) \left( \cos\left(\frac{2z}{L}\right) + 2 \right). \end{aligned}$$

In the computation,  $L = 1$ ,  $V_0 = 1$ ,  $\rho_0 = 1$ , and the Mach number takes  $M_0 = V_0/c_0 = 0.1$ , where  $c_0$  is the sound speed. The fluid is a perfect gas with  $\gamma = 1.4$ , Prandtl number is  $Pr = 0.71$ , and Reynolds number  $Re = 1600$ . The characteristic convective time  $t_c = L/V_0$ . This problem is aimed at the performance of high-order gas-kinetic scheme on the direct numerical simulation of nearly incompressible turbulent flows. In the computation, the cases  $TG_1$ ,  $TG_2$ ,  $TG_3$  and  $TG_4$  with  $128^3$ ,  $256^3$ ,  $512^3$  and  $1024^3$  uniform cells are tested, and the numerical results of BB13 dispersion relation preserving (DRP) scheme [39] with  $512^3$  cells are given as reference [33]. The BB13 scheme was originally developed for noise computations, in which a high-order finite difference method equipped with fourth-stage third-order algorithm for time discretization and 13-point stencils for spatial discretization. The compressible Navier-Stokes equations are solved by both high-order gas-kinetic scheme and finite difference method.

To test the performance of HGKS, several diagnostic quantities are computed from the flow as it evolves in time. The volume-averaged kinetic energy is given by

$$E_k = \frac{1}{\rho_0 \Omega} \int_{\Omega} \frac{1}{2} \rho \mathbf{U} \cdot \mathbf{U} d\Omega,$$

where  $\Omega$  is the volume of the computational domain. The dissipation rate of kinetic energy can be computed by the temporal derivative of  $E_k$

$$\varepsilon(E_k) = -\frac{dE_k}{dt},$$

which is computed by second order central difference in the numerical results of  $E_k$ . For the incompressible limit, the dissipation rate is related to the integrated enstrophy by

$$\varepsilon(\zeta) = 2 \frac{\mu}{\rho_0} \zeta,$$

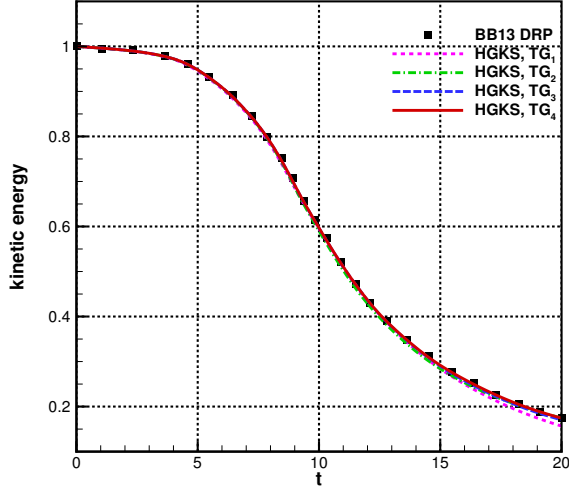


Figure 2: Taylor-Green vortex: time history of kinetic energy  $E_k$ .

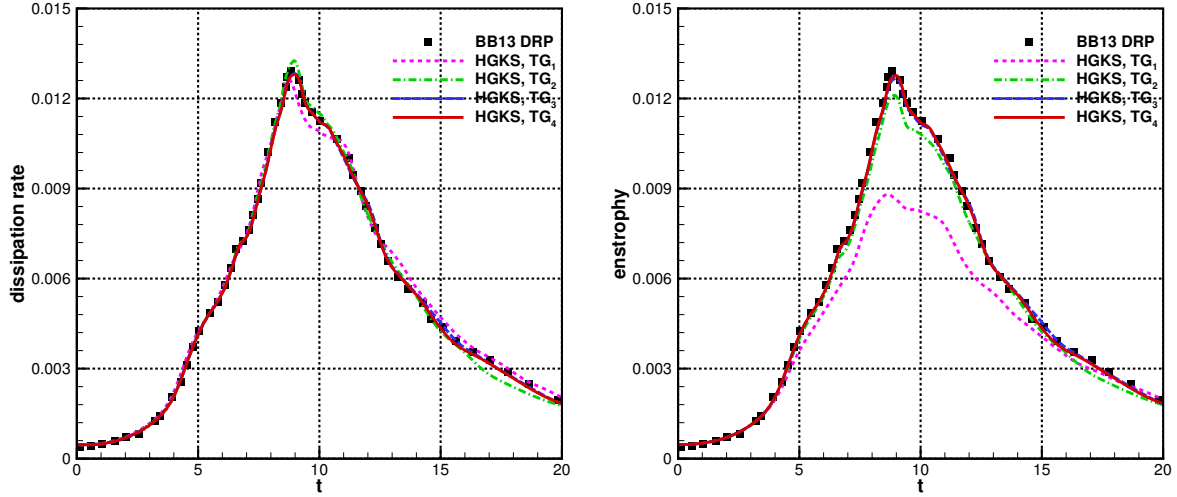


Figure 3: Taylor-Green vortex: time history of dissipation rate  $\varepsilon(E_k)$  and enstrophy  $\varepsilon(\zeta)$ . The reference data is  $\varepsilon(E_k)$  with  $512^3$  cells for two contours [33].

where  $\mu$  is the coefficient of viscosity,  $\boldsymbol{\omega} = \nabla \times \boldsymbol{U}$  and

$$\zeta = \frac{1}{\rho_0 \Omega} \int_{\Omega} \frac{1}{2} \rho \boldsymbol{\omega} \cdot \boldsymbol{\omega} d\Omega.$$

The time history of kinetic energy is shown in Fig.2, where the reasonable agreement is observed with the reference solution except for the simulation with  $128^3$  cells. The kinetic energy dissipation rates  $\varepsilon(E_k)$  and the enstrophy integral computed  $\varepsilon(\zeta)$  are shown in Fig.3, respectively. A large discrepancy is observed in the peak dissipation rate for  $\varepsilon(E_k)$  and

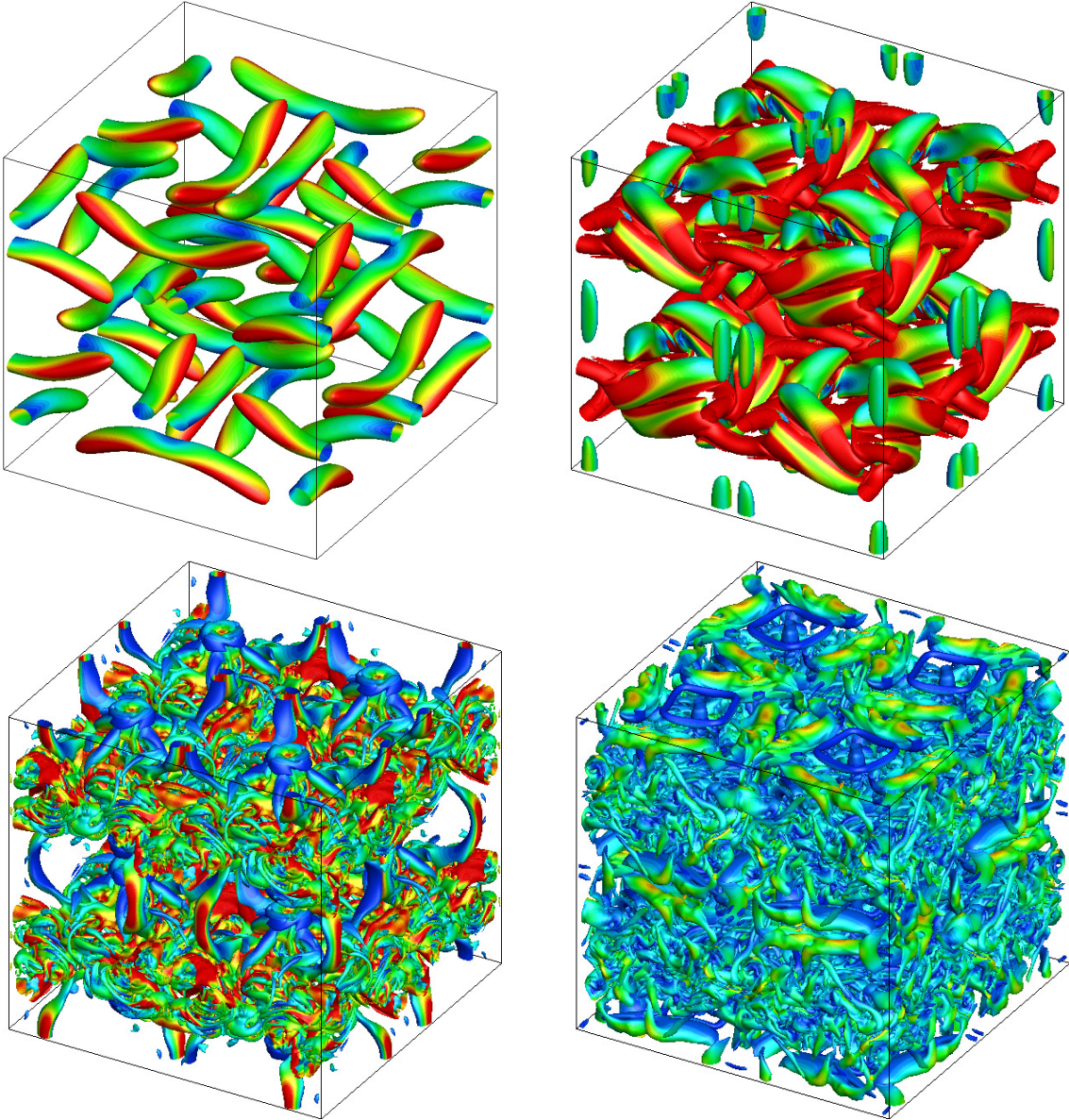


Figure 4: Taylor-Green vortex: iso-surface of the second invariant of velocity gradient tensor  $Q_v = -0.5$  at  $t = 2.5, 5, 10$  and  $15$  colored by velocity magnitude.

$\varepsilon(\zeta)$  with  $128^3$  cells and  $256^3$  cells, and an excellent agreement with the reference solution is obtained with the mesh refinement. Especially, the mesh with  $1024^3$  cells is the finest resolution for the Taylor-Green vortex problem, and a benchmark results have been provided. As time evolves, the vortex roll-up, stretch and interact, eventually breaking down into turbulence. The iso-surface of the second invariant of velocity gradient tensor  $Q_v$ , colored by velocity magnitude at  $t = 2.5, 5, 10$  and  $15$  with  $512^3$  cells are shown in Fig.4. Velocity magnitude ranges from 0 to 0.2 and 20 equivalent levels are used. At the earliest time, the flow behaves inviscidly as the vortex begin to evolve and roll-up. At  $t = 10$ , the coherent

structures breakdown. Beyond this breakdown, the flow is fully turbulent and the structures slowly decay until the flow comes to rest. The results indicate that the resolution of HGKS is comparable even with the higher-order finite difference method, which is widely used in DNS of turbulence.

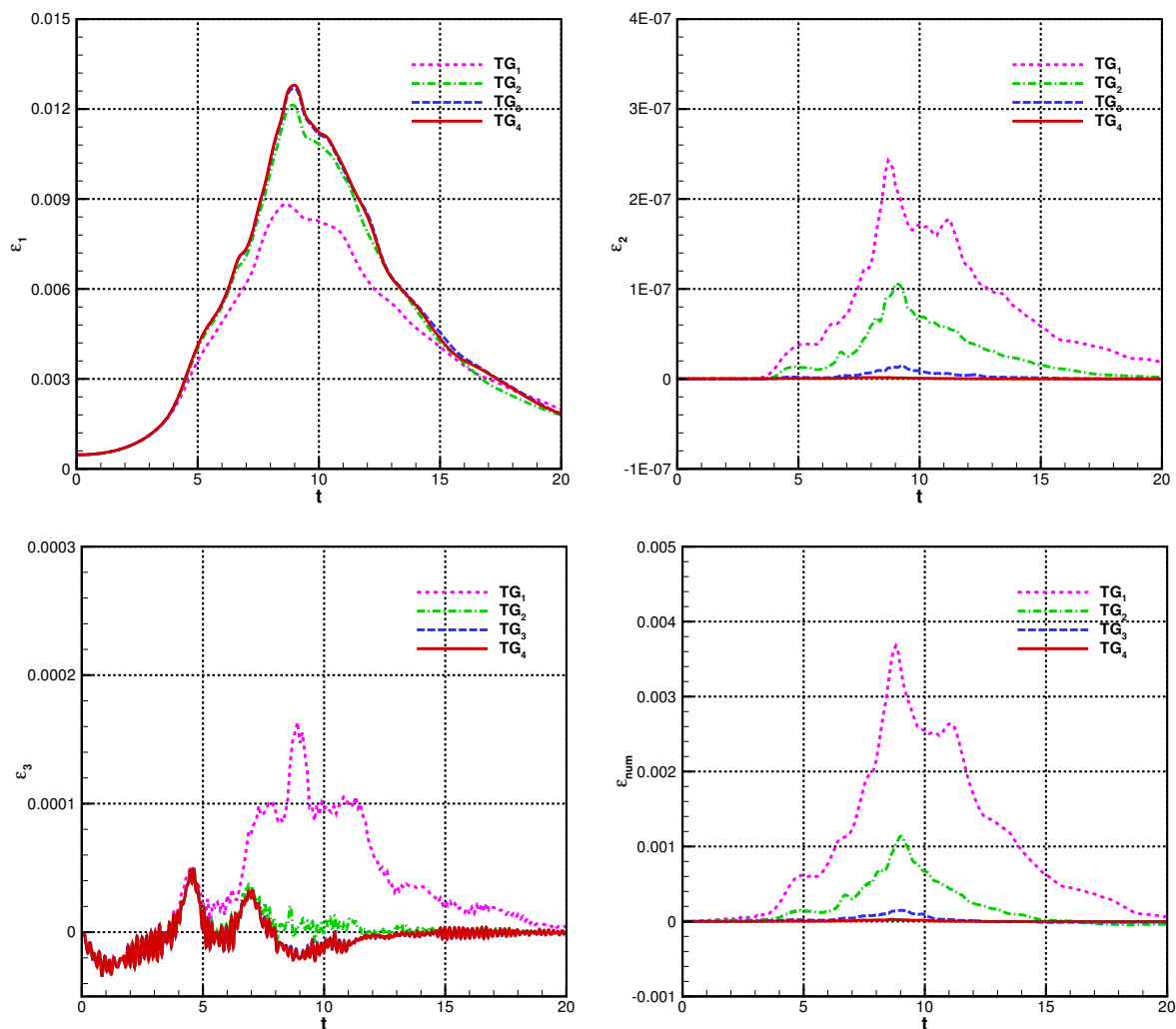


Figure 5: Taylor-Green Vortex: the time history of  $\varepsilon_1$ ,  $\varepsilon_2$ ,  $\varepsilon_3$  and  $\varepsilon_{num}$ .

In the numerical simulation, the final dissipative behavior is determined by both physical and numerical dissipation. For the current study, the quantitative study of numerical dissipation is presented as well, which is less reported in literatures. For the compressible flow, the kinetic energy dissipation rate obtained from the Navier-Stokes equations is the

sum of three contributions, namely,

$$\begin{aligned}\varepsilon_1 &= 2\frac{\mu}{\rho_0}\frac{1}{\Omega}\int_{\Omega}\mathbf{S}^d:\mathbf{S}^d d\Omega, \\ \varepsilon_2 &= \frac{\mu_b}{\rho_0}\frac{1}{\Omega}\int_{\Omega}(\nabla\cdot\mathbf{U})^2 d\Omega, \\ \varepsilon_3 &= -\frac{1}{\rho_0\Omega}\int_{\Omega}p\nabla\cdot\mathbf{U} d\Omega,\end{aligned}$$

where  $\mathbf{S}^d$  is the deviatoric part of the strain rate tensor,  $\mu_b$  is the bulk viscosity. In current scheme, the inherent bulk viscosity [20] reads

$$\mu_b = \frac{2N}{3(N+3)}\mu,$$

where  $N = 2$  for the diatomic gas. The contributions to the dissipation rate based on the compressible flow assumptions are shown in Fig.5. To eliminate the error from numerical discretization, all spatial derivatives are computed by sixth order central difference for three components of dissipation rate. As expected, the primary contribution  $\varepsilon_1$  is almost identical to  $\varepsilon(\zeta)$  in current nearly incompressible simulation, and the bulk viscosity contribution  $\varepsilon_2$  and dilatation contribution  $\varepsilon_3$  can be neglected. It is noted that the magnitude of pressure dilation term  $\varepsilon_3$  is on the same order as that of the reference solution [33]. With coarse mesh resolutions, the total dissipation rate computed from  $\varepsilon_1 + \varepsilon_2 + \varepsilon_3$  is significantly lower than  $\varepsilon(E_k)$ . Therefore, the numerical dissipation can be quantitatively computed by

$$\varepsilon_{\text{num}} = \varepsilon(E_k) - (\varepsilon_1 + \varepsilon_2 + \varepsilon_3).$$

The time history of numerical dissipation is given in Fig.5 as well. With the refinement of grid, the resolution of the vortical structures increases and the effect of the filtering decreases, which reduces numerical dissipation. The fact that  $\varepsilon(E_k)$  is well predicted at all grid levels indicates that the physical and numerical dissipation work together consistently in the calculation to get the final "physical" result. In other words, the filtering due to the coarse mesh correctly mimics the physical dissipation from the unresolved scale dynamics. This validates the usage of high-order numerical methods for the implicit large-eddy simulations (iLES) [40]. While the iLES for complex turbulent flows is still under debate, the current quantitative analysis of numerical dissipation gives the specific hints on this issue.

### 3.2. Efficiency test of parallel computation

In this section, the efficiency of parallel computation is tested in the above Taylor-Green vortex problem. To give the performance of parallel computation, the speedup is defined as

$$S_n = \frac{T_n}{T_{n_{\text{ref}}}},$$

where  $T_n$  is the execution time with  $n$  cores and  $T_{n_{\text{ref}}}$  is the execution time on a reference number of processors. The ideal speedup of parallel computations would be equal to  $n/n_{\text{ref}}$ . With the log-log plot for  $n$  and  $T_n$ , an ideal scalability would follow  $-1$  slope. However, this efficiency is not possible due the communication delay among the computational cores and the idle time of computational nodes associated with load balancing. The scalability of our MPI code is examined by measuring the wall clock time against the number of processors. The detailed performance of MPI parallel computing is given in Table.1 and a log-log plot is also given in Fig.6, where 4, 16 and 64 cores for  $256^3$  cells, and 64, 256, and 1024 cores are used for  $512^3$  cells. Total 30 steps are computed for each case, and CPU time is the averaged time for each step. The code was run on the TianHe-II, and the node details are presented in Table.2. Due to the explicit formulation of HGKS, our MPI code scales properly with the number of processors used. It is indicated that the data communication crossing nodes costs a little time and the computation for flow field is the dominant one.

Grid size	Cores	CPU time (s/step)	Grid size	Cores	CPU time (s/step)
$256^3$	4	121.01	$512^3$	64	69.00
$256^3$	16	34.08	$512^3$	256	17.29
$256^3$	64	9.09	$512^3$	1024	4.66

Table 1: Efficiency test of parallel strategy: detailed CPU time against number of core.

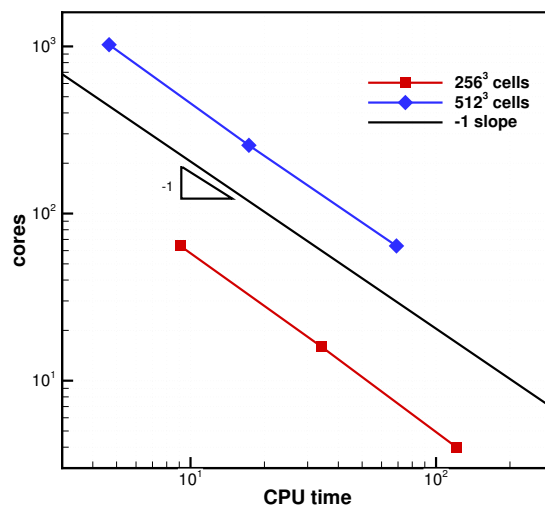


Figure 6: Efficiency test of parallel strategy: log-log plot for  $n$  and  $T_n$ .

For most DNS, the high-order finite difference method is widely used, and the finite volume scheme is rarely applied due to the complicated formulation. Because of the procedure of multidimensional spatial reconstruction and quadrature of numerical fluxes at cell interface, the finite volume scheme is considered to be less efficient than the finite difference

System	Node type	Cache	Host channel adapter
TianHe-II	Intel Xeon E5-2692 (2.2GHz/core)	30MB	InfiniBand
Pleiades	Intel Xeon E5-2670 (2.6GHz/core)	20MB	InfiniBand

Table 2: Efficiency test of parallel strategy: node details for TianHe-II and Pleiades supercomputer systems.

method. For the high-order gas-kinetic scheme, the gas-kinetic flux solver Eq.(5) considered to be even more complicated than Riemann solvers [22], which is usually used in the classical finite volume scheme. In this case, the comparison of total computational cost with the finite difference method is also given. The time step and total computational costs of HGKS are presented in Table.3, in which the current HGKS is running on the TianHe-II supercomputer system. As reference, the efficiency of high-order finite difference method [33] is given in Table.4, in which the cases were run on the NASA Pleiades high performance computing system. The node details are compared in Table.2, and the total computational costs of HGKS is around 1.4 times higher than the finite difference method. In addition, considering the processor speed, the HGKS is around 1.2 times higher than the finite difference method. Taken the robustness of HGKS into account, such computational cost is comparable and affordable.

Case	Grid size	Time step	Cores	Hours	Computational costs
$TG_1$	$128^3$	$1.785 \times 10^{-3}$	16	13.3	213 core hours
$TG_2$	$256^3$	$8.925 \times 10^{-4}$	256	13.5	3456 core hours
$TG_3$	$512^3$	$4.462 \times 10^{-4}$	1024	66	67584 core hours
$TG_4$	$1024^3$	$2.789 \times 10^{-4}$	1024	730	747062 core hours

Table 3: Efficiency test of parallel strategy: detailed computational parameters for HGKS.

Grid size	Time step	Cores	Hours	Computational costs
$256^3$	$8.463 \times 10^{-4}$	64	40	2560 core hours
$512^3$	$4.231 \times 10^{-4}$	368	130	47840 core hours

Table 4: Efficiency test of parallel strategy: detailed computational parameters for BB13 [33].

### 3.3. Turbulent channel flow

Considering the simplicity of geometry and boundary conditions, the turbulent channel flows have been studied to understand the mechanism of wall-bounded turbulent flows. A large number of computational studies of turbulent channel flows have been carried out [3, 42, 4]. In the current study, the turbulent channel flow with friction Reynolds number  $Re_\tau = 180$  is tested. In the computation, the physical domain is  $(x, y, z) \in [0, 2\pi] \times [-1, 1] \times [0, \pi]$  and the computational domain takes  $(\xi, \eta, \zeta) \in [0, 2\pi] \times [0, 3\pi] \times [0, \pi]$ . The coordinate

transformation is given by

$$\begin{cases} x = \xi, \\ y = \tanh(b_g(\frac{\eta}{1.5\pi} - 1)) / \tanh(b_g), \\ z = \zeta, \end{cases}$$

where  $b_g = 2$ . The periodic boundary conditions are used in streamwise  $x$ -direction and spanwise  $z$ -directions, and the non-slip and isothermal boundary conditions are used in vertical  $y$ -direction. The fluid is initiated with  $\rho = 1$ ,  $Ma = 0.1$  and the initial streamwise velocity profile is given by the perturbed Poiseuille flow profile

$$U(y) = 1.5(1 - y^2) + \text{white noise}.$$

White noise is added with 10% amplitude of local streamwise velocity. With the unit averaged streamwise velocity, the initial pressure can be given. The friction Reynolds number is defined as

$$Re_\tau = \rho u_\tau H / \mu,$$

where  $H = 1$  is the half height of the channel and the frictional velocity  $u_\tau$  is given by

$$u_\tau = \sqrt{\frac{\tau_{wall}}{\rho}}, \quad \tau_{wall} = \frac{\partial U}{\partial y} \Big|_{wall}.$$

For the channel flow, the logarithmic formulation is given by

$$U^+ = \frac{1}{\kappa} \ln Y^+ + B, \quad (8)$$

where von Karman constant  $\kappa = 0.40$  and  $B = 5.5$  for the low Reynolds number turbulent channel flow [3]. The plus unit and plus velocity are defined as

$$Y^+ = \rho u_\tau y / \mu, \quad U^+ = U / u_\tau.$$

Therefore, the plus velocity  $U_c^+ = 18.4823$  at center line of the channel according to Eq.(8), where  $Y_c^+ = 180$  at center line. The frictional velocity is determined by  $u_\tau = U_c / U_c^+ = 0.0541$ , where  $U_c = 1$  is the centreline line velocity. In this computation, the cases  $G_1$  and  $G_2$  are tested, where  $96^3$  and  $128^3$  cells are distributed uniformly in computational space. 256 cores and 1024 cores are used to simulate the  $G_1$  and  $G_2$ , respectively. The details of mesh are given in Table.5, where  $\Delta y_{min}^+$  and  $\Delta y_{max}^+$  are the minimum and maximum grid space in the  $y$ -direction. To resolve the viscous layer, there are 11 layers for  $G_1$  and 15 layers for  $G_2$  within  $Y^+$  less than 10, respectively. As reference, the mesh and initial streamwise velocity in the physical domain for  $G_1$  are given in Fig.7.

To excite channel flow from laminar to turbulence, an external force is exerted in the

Case	Grid size	$\Delta y_{min}^+/\Delta y_{max}^+$	$\Delta x^+$	$\Delta z^+$
$G_1$	$96^3$	0.29/7.77	11.77	5.89
$G_2$	$128^3$	0.21/5.83	8.83	4.42

Table 5: Turbulent channel flow: different sets of grids for  $Re_\tau = 180$  turbulent channel flow.

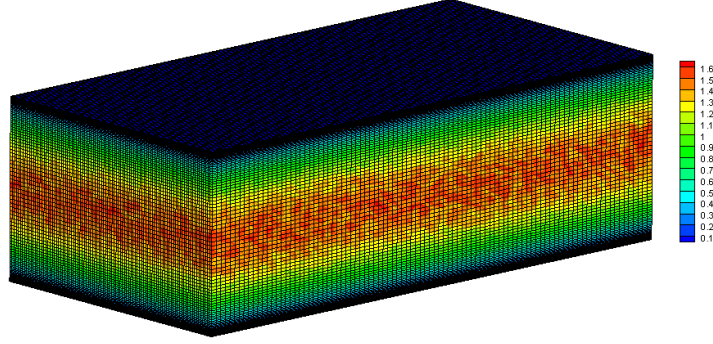


Figure 7: Turbulent channel flow: the mesh and initial streamwise velocity distributions for case  $G_2$ .

streamwise direction. According to the viscous layer  $U^+ = Y^+$ , a fixed nondimensional external force can be approximated by balance of forces

$$f_x = \tau_{wall}/H = 2.93 \times 10^{-3}.$$

Before transition, the external force  $f_x \cdot \Delta t$  and  $10f_x \cdot \Delta t$  are used for  $G_1$  and  $G_2$ , respectively.  $\Delta t$  is the time step. After transition, the constant moment flux is used to determine the external force. According to the experiment and previous work [3, 34], the constant bulk volume is recommended to be set as

$$\iiint_{\Omega} (\rho U)_{ijk}^{n+1} d\Omega = \iiint_{\Omega} (\rho U_b) d\Omega,$$

where  $U_c/U_b = 1.16$  is chosen based on previous DNS [3]. The conservative variables updated by the two-stage method Eq.(6) are denoted as  $\tilde{Q}^{n+1}$  and the conservative variables with external force is  $Q^{n+1}$ . With the external force, the equation for momentum in streamwise direction and energy can be written as

$$\begin{aligned} \frac{\partial \rho U}{\partial t} &= \mathcal{L}_{\rho U} + \rho f_x, \\ \frac{\partial \rho E}{\partial t} &= \mathcal{L}_{\rho E} + \rho U f_x, \end{aligned}$$

where  $\mathcal{L}_{\rho U}, \mathcal{L}_{\rho E}$  are the operator for spatial derivative of momentum and energy fluxes and

$f_x$  is the external force, which can be given as follows

$$f_x = \frac{1}{\Delta t} \cdot \frac{\iiint_{\Omega} (\rho U)_{ijk}^{n+1} d\Omega - \iiint_{\Omega} (\widetilde{\rho U})_{ijk}^{n+1} d\Omega}{\frac{1}{2} \iiint_{\Omega} (\rho_{ijk}^n + \widetilde{\rho}_{ijk}^{n+1}) d\Omega}.$$

and the equation for momentum in streamwise direction and energy can be updated

$$\begin{aligned} (\rho U)_{ijk}^{n+1} &= (\widetilde{\rho U})_{ijk}^{n+1} + \frac{1}{2} \Delta t (\rho_{ijk}^{n+1} + \rho_{ijk}^n) f_x, \\ (\rho E)_{ijk}^{n+1} &= (\widetilde{\rho E})_{ijk}^{n+1} + \frac{1}{2} \Delta t ((\rho U)_{ijk}^{n+1} + (\rho U)_{ijk}^n) f_x. \end{aligned}$$

Therefore, the momentum flux over the whole domain keeps constant in the computation. The external force before the transition and after transition with grid  $G_1$  and  $G_2$  are presented in Fig.8. After over 500 characteristic periodic time as  $500H/U_c$ , it can be seen that the initial laminar flow-fields transit to turbulence. Then, the external force based on the constant moment flux are used. The total stress is used to test whether the simulated turbulence is statistically stationary [1, 4]. In a statistically stationary turbulent channel, the total stress, which is the sum of Reynolds stress and mean viscous stress, is linear because of momentum conservation

$$\frac{dU^+}{dY^+} - \langle UV \rangle^+ \approx 1 - \frac{Y^+}{Re_{\tau}}.$$

When the residual of total stress converging, the 350 periodic time as  $350H/U_c$  is used, which is comparable to that in the reference paper [41, 42]. As shown in Fig.9, the residual is less than 2.6% for case  $G_1$  and 1.2% for case  $G_2$ .

Case	$Re_{\tau}$	$Re_c$	$Re_b$	$C_f$
$G_1$	176.03	3297.78	5720.09	$7.58 \times 10^{-3}$
$G_2$	179.21	3319.22	5730.11	$7.82 \times 10^{-3}$

Table 6: Turbulent channel flow: mean flow variables for case  $G_1$  and  $G_2$ .

The mean flow variables with different sets of grids are presented in Table.6.  $Re_{\tau}$  is the averaged friction Reynolds number,  $U_c$  is the averaged mean centerline velocity,  $U_b$  is the averaged mean bulk velocity.  $Re_c = U_c H / \nu$ ,  $Re_b = U_b 2H / \nu$ ,  $C_f = \tau_{wall} / (\rho U_b^2 / 2)$ , and  $C_f$  is the skin friction coefficients. The result on  $G_2$  is much closer with Dean's suggested correlation of  $C_f = 0.073 Re_b^{-0.25} = 8.39 \times 10^{-3}$  [43]. The averaged velocity profiles with grid  $G_1$  and  $G_2$  are presented in Fig.10. The first DNS of fully developed incompressible turbulent channel flow was performed by the spectral method with  $129 \times 192 \times 160$  grids [3]. As the most popular mesoscopic methods for simulating nearly incompressible flows, the numerical results of the LBM with  $200 \times 400 \times 200$  grids and DUGKS with  $128^3$  grids

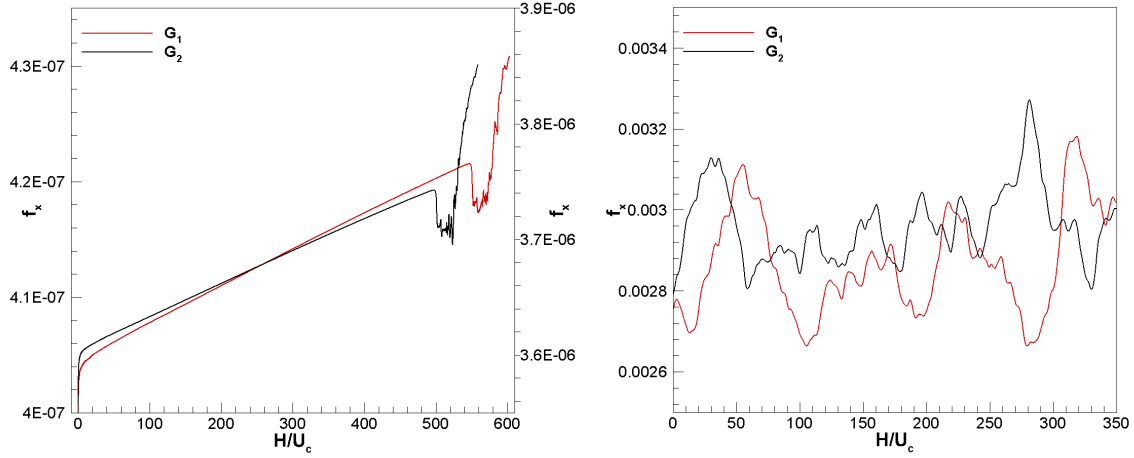


Figure 8: Turbulent channel flow: time evolution of the external force for case  $G_1$  and  $G_2$ .

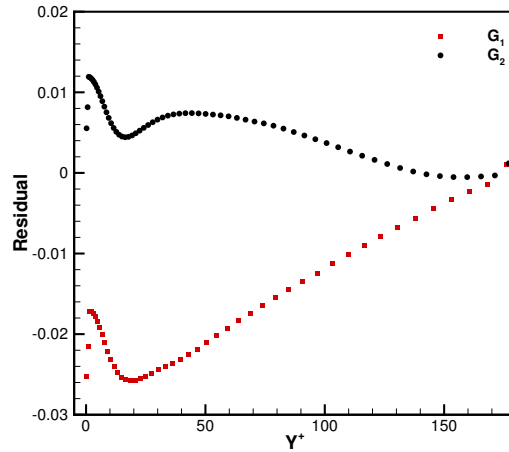


Figure 9: Turbulent channel flow: distribution of stress residual for case  $G_1$  and  $G_2$ .

are also presented [34], in which the physical accuracy has been demonstrated by comparing with the Navier-Stokes based spectral methods. The mean flow velocity with a log-linear plot and a local enlargement are given in Fig.10, where the HGKS result is in reasonable agreement with the spectral results, LBM and DUGKS results.

The averaged Reynolds shear stress profiles are shown in Fig.11 in linear-linear and log-linear plots. The sum of Reynolds stress and viscous stress varies linearly from the channel center to the channel wall. When compared to the spectral result, HGKS results are clearly better than DUGKS and LBM results, especially in the near-wall region. Turbulence intensities, i.e., the root-mean-square (rms) velocity profiles are shown in Fig.12 as well. In the near-wall regions, the streamwise rms velocity is the largest and the spanwise rms velocity is the smallest. DUGKS yields a better result for  $U_{rms}^+$  in the near-wall region.

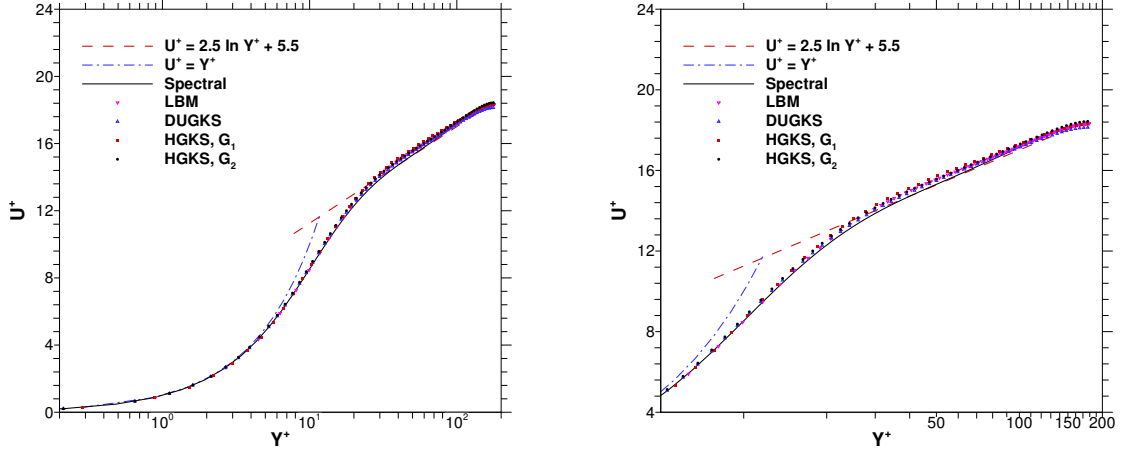


Figure 10: Turbulent channel flow: mean flow velocity profiles and the local enlargement.

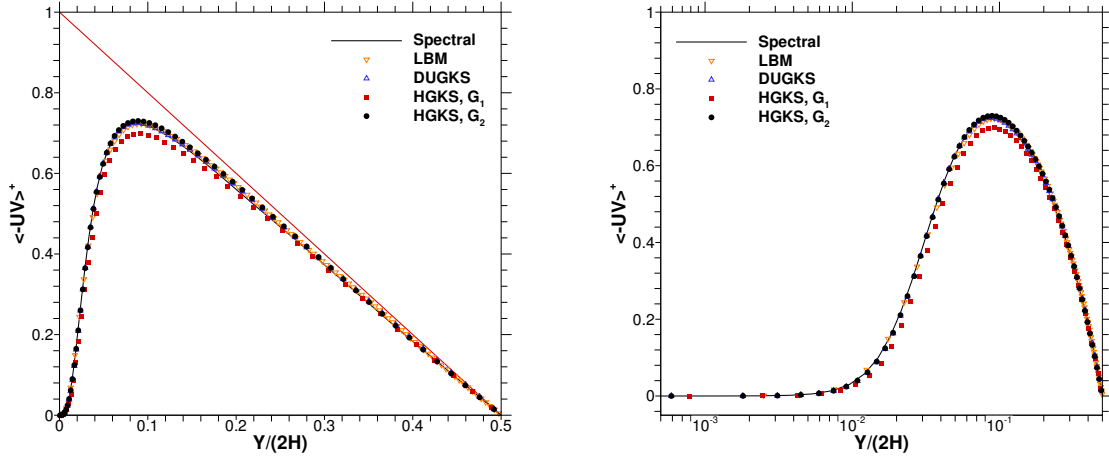


Figure 11: Turbulent channel flow: Reynolds stress profiles in linear-linear and log-linear plots.

Meanwhile, for  $V_{rms}^+$  and  $W_{rms}^+$ , LBM behaves better in the near-center line region, and DUGKS behaves better in the near-wall region. Considering the good agreement in near-wall region and the near-center line region with the spectral benchmark, it is clear that HGKS outweighs LBM and DUGKS. The relative error in DUGKS is due only to the numerical truncation error, while the relative error in LBM is due to both the domain size effect and numerical truncation error [34]. Different distribution of grid points in the spanwise direction and different grid resolutions should be tested, which could be a topic of HGKS for turbulent channel flows. Finally, the limiting wall behavior of the Reynolds stresses is shown in Table.7, where  $A_1 = U_{rms}^+/Y^+$ ,  $B_1 = V_{rms}^+/Y^{+2} \times 10^2$ ,  $C_1 = W_{rms}^+/Y^+$  and  $D_1 = \langle -UV \rangle^+/Y^{+3} \times 10^3$ . The  $y$  behavior of tangential stresses  $U_{rms}^+$  and  $W_{rms}^+$  and

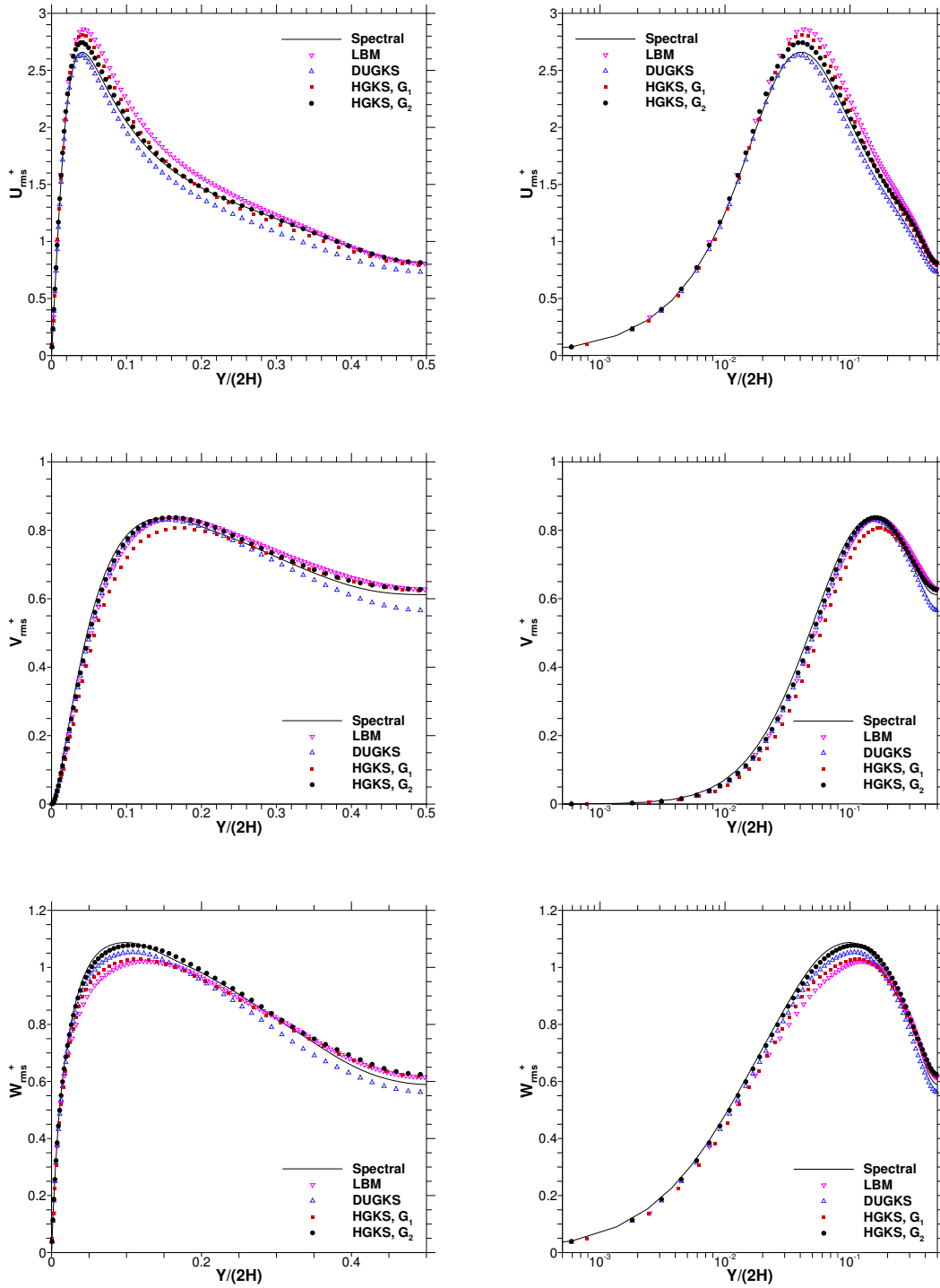


Figure 12: Turbulent channel flow: root-mean-square fluctuation velocity profiles in linear-linear and log-linear plots.

the  $y^2$  behavior of normal stress  $V_{rms}^+$  are expected from consideration of no-slip boundary conditions and continuity equation. Reynolds shear stress  $\langle -UV \rangle^+$  is in the asymptotic behavior of  $y^3$ , which is regarded as the benchmark to calibrate the asymptotic near-wall behavior of eddy-viscosity turbulence models [44]. Currently, the magnitudes of  $A_1$ ,  $B_1$ ,  $C_1$  and  $D_1$  are in good agreement with the results with spectral method [3].

$Y^+$	$A_1$	$B_1$	$C_1$	$D_1$
0.2124	0.3579	0.8891	0.1839	0.7827
0.6505	0.3624	0.7207	0.1762	0.7046
1.1157	0.3628	0.6568	0.1678	0.7015
1.6096	0.3624	0.6117	0.1594	0.7065
2.1338	0.3614	0.5716	0.1512	0.7088
2.6902	0.3595	0.5343	0.1432	0.7055
3.2807	0.3564	0.4990	0.1353	0.6947
4.5715	0.3518	0.4656	0.1278	0.6756
5.2761	0.3453	0.4339	0.1205	0.6479

Table 7: Turbulent channel flow: near-wall behavior of Reynolds stresses for case  $G_1$ .

In summary, the first simulation of turbulent channel flow using HGKS shows that the results are reasonably accurate, and performance is better than the second-order LBM and DUGKS. More importantly, the HGKS results are obtained with a coarse grid resolution covering a large domain size compared with LBM. As the equidistant grids are required for LBM, the grids displacement is limited to an extreme small value to resolve the viscous layer, i.e.,  $\Delta x^+ \approx 0.3$  in the whole computational domain, so the required grids number of LBM will exceed HGKS dramatically. In the current computation, the spatial reconstruction is based on the WENO reconstruction on uniform meshes due to the small variation of neighboring cells, and the order of accuracy may be affected slightly. Currently, we are working on the genuinely high-order gas-kinetic scheme on the nonuniform and curvilinear meshes, and the geometrical errors can be excluded in the future simulations.

### 3.4. Isotropic compressible turbulence

The isotropic compressible turbulence is regarded as one of cornerstones to elucidate the effects of compressibility for turbulence [10, 45]. Based on the numerical experiments and theoretical analysis, the isotropic compressible turbulence is divided into four main dynamical regimes, i.e. the low-Mach number quasi-isentropic regime, the low-Mach number thermal regime, the nonlinear subsonic regime, and the supersonic regime [11]. High-order compact finite difference method [15] has been widely utilized in the simulation of isotropic compressible turbulence with moderate turbulent Mach number, i.e.  $Ma_t \leq 0.8$ . However, when simulating the turbulent in supersonic regime, the compact scheme fails to capture strong shocklets and suffers from numerical instability. In this case, we concentrate on the decaying isotropic compressible turbulence without external force. The flow domain of numerical simulation is a cube box  $0 \leq x, y, z \leq 2\pi$ , with periodic boundary conditions in

all three Cartesian directions for all flow variables. A three-dimensional solenoidal random initial velocity field  $\mathbf{U}$  is generated by a specified spectrum [46]

$$E(\kappa) = A_0 \kappa^4 \exp(-2\kappa^2/\kappa_0^2), \quad (9)$$

where  $A_0$  is a constant to get a specified initial kinetic energy,  $\kappa$  is the wave number,  $\kappa_0$  is the wave number at which the spectrum peaks. In this paper, fixed  $A_0$  and  $\kappa_0$  in Eq.(9) are chosen for all cases, which are initialized by  $A_0 = 0.00013$  and  $\kappa_0 = 8$ . Evolution of this artificial system is determined by initial thermodynamic quantities and two dimensionless parameters, i.e. the initial Taylor microscale Reynolds number and turbulent Mach number

$$Re_\lambda = \frac{(2\pi)^{1/4} \rho_0}{4 \mu_0} \sqrt{2A_0 \kappa_0^3},$$

$$Ma_t = \frac{\sqrt{3}}{\sqrt{\gamma R T_0}} u_{rms},$$

where the initial density  $\rho_0 = 1$  and  $U_{rms}$  is the root mean square of initial velocity field

$$U_{rms} = \left\langle \frac{\mathbf{U} \cdot \mathbf{U}}{3} \right\rangle^{1/2}.$$

With  $Re_\lambda$ ,  $Ma_t$  and  $\gamma = 1.4$ , the initial viscosity  $\mu_0$ , pressure  $p_0$  and temperature  $T_0$  can be determined. The dynamic velocity can be also given by

$$\mu = \mu_0 \left( \frac{T}{T_0} \right)^{0.76}.$$

With current initial strategy, the initial ensemble turbulent kinetic energy  $K_0$ , ensemble enstrophy  $\Omega_0$ , ensemble dissipation rate  $\varepsilon_0$ , large-eddy-turnover time  $\tau_{to}$ , Kolmogorov length scale  $\eta_0$ , and the Kolmogorov time scale  $\tau_0$  are given as

$$K_0 = \frac{3A_0}{64} \sqrt{2\pi} \kappa_0^5, \quad \Omega_0 = \frac{15A_0}{256} \sqrt{2\pi} \kappa_0^7, \quad \tau_{to} = \sqrt{\frac{32}{A_0}} (2\pi)^{1/4} \kappa_0^{-7/2},$$

$$\varepsilon_0 = 2 \frac{\mu_0}{\rho_0} \Omega_0, \quad \eta_0 = (\nu_0^3/\varepsilon_0)^{1/4}, \quad \tau_0 = (\nu_0/\varepsilon_0)^{1/2}. \quad (10)$$

For the compressible isotropic turbulence, starting from the initial flows, the large eddies transfer their turbulent kinetic energy successively to smaller eddies. The time history of the root-mean-square density fluctuation  $\rho_{rms}(t)$ , turbulent kinetic energy  $K(t)$ , skewness

factor  $S_u(t)$  and flatness factor  $F_u(t)$  for velocity slope are defined as

$$\begin{aligned}\rho_{rms}(t) &= \sqrt{\langle(\rho - \bar{\rho})^2\rangle}, \\ K(t) &= \frac{1}{2} \langle \rho \mathbf{U} \cdot \mathbf{U} \rangle, \\ S_u(t) &= \sum_i \frac{\langle(\partial_i U_i)^3\rangle}{\langle(\partial_i U_i)^2\rangle^{3/2}}, \\ F_u(t) &= \sum_i \frac{\langle(\partial_i U_i)^4\rangle}{\langle(\partial_i U_i)^2\rangle^2}.\end{aligned}$$

In this process, the evolution of turbulent kinetic energy is of interest since it is a fundamental benchmark for incompressible and compressible turbulence modeling [47, 2]. The decay of the ensemble turbulent kinetic energy can be described approximately by [10]

$$\begin{aligned}\frac{d\langle K \rangle}{dt} &= \varepsilon + \langle p\theta \rangle, \\ \varepsilon &= \varepsilon_s + \varepsilon_d,\end{aligned}\tag{11}$$

where  $\varepsilon_s = \langle \mu \omega_i \omega_i \rangle$  is the ensemble solenoidal dissipation rate,  $\varepsilon_d = 4/3 \langle \mu \theta^2 \rangle$  is the ensemble dilational dissipation rate,  $\langle p\theta \rangle$  is the ensemble pressure-dilation transfer,  $\omega_i = \epsilon_{ijk} \partial U_k / \partial x_j$  is the fluctuating vorticity,  $\epsilon_{ijk}$  is the alternating tensor and  $\theta = \nabla \cdot \mathbf{U}$  is the fluctuating divergence of velocity.

Case	$Ma_t$	$dt_{ini}/\tau_{to}$	$\kappa_{max}\eta_0$	$\Delta/\eta_0$	$\Delta/\lambda_0$
$R_1$	0.8	1.04/1000	3.613	0.819	2.551
$R_2$	1.0	1.09/1000	3.613	0.819	2.041
$R_3$	1.2	1.14/1000	3.613	0.819	1.700
$R_4$	1.6	1.19/1000	3.613	0.819	1.275

Table 8: Isotropic compressible turbulence: parameters for different high turbulent Mach number.

Due to the robustness of current scheme, we can simulate this case up to the supersonic regime, which is seldom reported in literatures. The WENO-Z scheme [14] used for the spatial reconstruction, no extra special treatment is needed in the code. In this case, the numerical tests  $R_1$ ,  $R_2$ ,  $R_3$  and  $R_4$  are presented with a fixed Taylor micro-scale Reynolds number  $Re_\lambda = 72$  to and the turbulent Mach number form  $Ma_t = 0.8$  to  $Ma_t = 1.6$ . In the computation, 256 cores are used for  $512^3$  uniform cells, and more parameters are given in Table.8, where  $\lambda_0$  is the initial mean free path approximated by  $\mu_0 = 1/3\rho_0 c_0 \lambda_0$  [35],  $\Delta$  is the uniform grid size in each direction,  $\eta_0$  is the initial Kolmogorov length scale as in Eq.(10),  $\kappa_{max} = \sqrt{2}\kappa_0 N/3$  is the maximum resolved number wave number,  $\kappa_0 = 8$  as Eq.(9) and  $N$  is the number of grid points in each Cartesian direction. The numerical tests show that the minimum spatial resolution parameter  $\kappa_{max}\eta_0 \geq 2.71$  and the maximum temporal resolution parameter  $\Delta t_{ini}/\tau_{to} \leq 5.58/1000$  for HGKS is adequate for resolving the isotropic

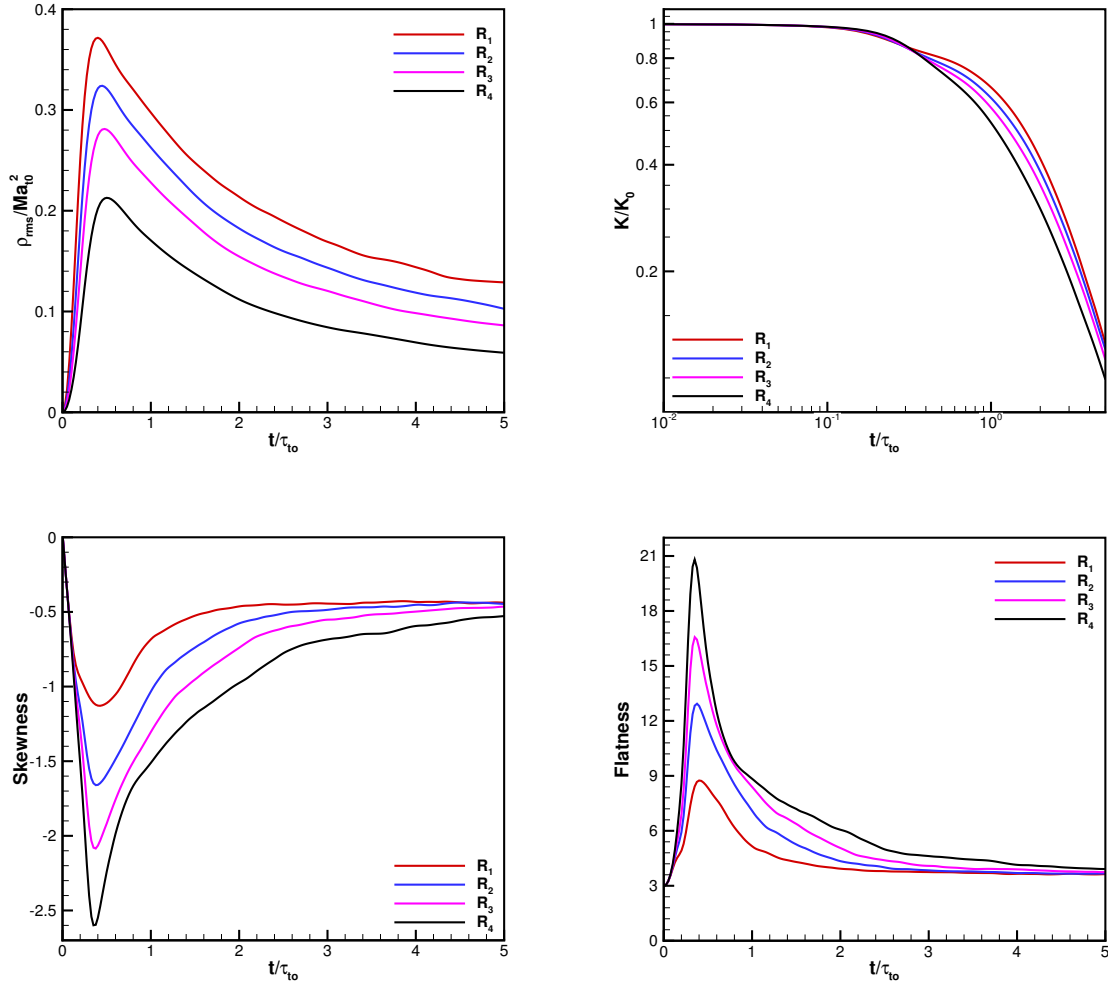


Figure 13: Isotropic compressible turbulence: time history of  $\rho_{rms}/Ma_t^2$ ,  $K/K_0$ ,  $S_u$ , and  $F_u$  for cases  $R_1$ - $R_4$ .

compressible turbulence [9]. According to Table.8, the Kolmogorov length scale is still larger than the mean free path, and each grid always contains more than one mean free path. This provides the intuitive evidence for controversial issue that smallest eddies in turbulence may still within the framework of continuum mechanics assumption.

Statistical quantities are provided for these cases, which provide benchmark solutions for supersonic isotropic compressible turbulence. Time history of  $\rho_{rms}(t)/Ma_t^2$ ,  $K(t)/K_0$ ,  $S_u(t)$  and  $F_u(t)$  are presented in Fig.14, which provides benchmark data for simulating isotropic compressible turbulence up to supersonic regime. The normalized root-mean-square density  $\rho_{rms}/Ma_t^2$  decreases monotonically with the increase of initial turbulent Mach number. With the increase of turbulent Mach number, the peak of skewness and flatness factor deviate from those of the low-Mach number thermal regime ( $Ma_t \leq 0.3$ ) severely. These large deviation

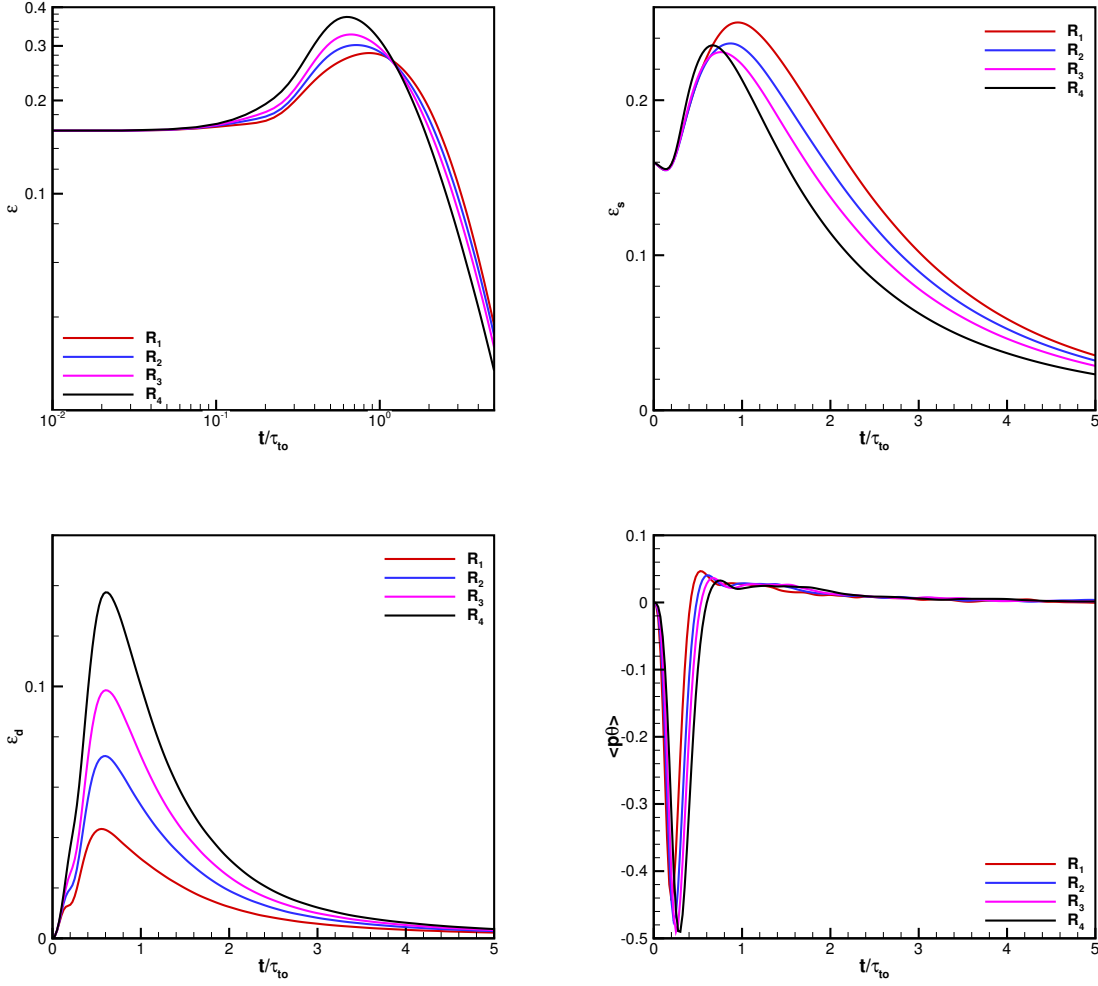


Figure 14: Isotropic compressible turbulence: time history of  $\varepsilon$ ,  $\varepsilon_s$ ,  $\varepsilon_d$  and  $\langle p\theta \rangle$  for cases  $R_1$ - $R_4$ .

indicates the most significant flow structures of isotropic compressible turbulence resulting from the shocklets. As the initial turbulent Mach number increases, the peak of dissipation increases as well. Obviously, ensemble solenoidal dissipation rate  $\varepsilon_s$  decreases with the increase of  $Ma_t$ , while the dilational dissipation rate  $\varepsilon_d$  rises with the increase of  $Ma_t$ . In addition,  $\langle p\theta \rangle$  changes signs during the evolution and preserves small but positive value thereafter, which agree with earlier study for subsonic isotropic turbulence [10]. During the early stage of the decaying supersonic isotropic turbulence, the ensemble pressure-dilation term can be in the same order of ensemble total dissipation rate. It is reported that the ratio between the ensemble pressure-dilation term and the right hand side of Eq.(11) becomes small for solenoidal forced quasi-stationary supersonic isotropic turbulence [48].

To investigate the behavior of supersonic isotropic compressible turbulence, the contours of normalized dilation  $\theta/\langle\theta\rangle^*$  on  $x = 0/y = 0/z = 0$  slices are presented in Fig.15 for

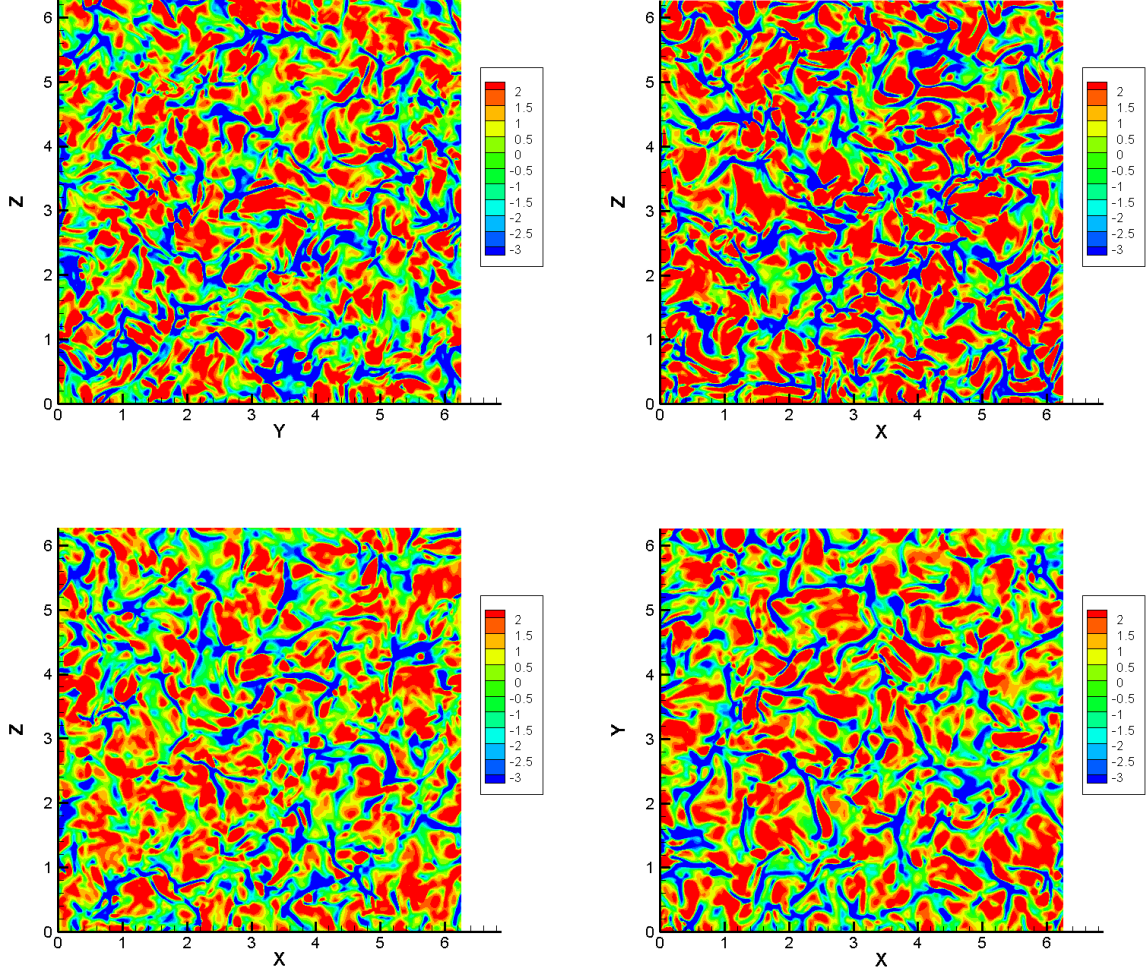


Figure 15: Isotropic compressible turbulence: contours of normalized dilation  $\theta / \langle \theta \rangle^*$  for cases  $R_1$ - $R_2$  at  $t/\tau_{to} = 1.0$ , and cases  $R_3$ - $R_4$  at  $t/\tau_{to} = 2.0$ .

four cases, where  $\langle \theta \rangle^*$  is root-mean-square dilation. Contours of normalized dilation show very different behavior between the compression motion and expansion motion. Strong compression regions  $\theta / \langle \theta \rangle^* \leq -3$  are usually recognized as shocklets [45]. In current study, shocklets behave in the shape of narrow and long ribbon, while high expansion regions  $\theta / \langle \theta \rangle^* \geq 2$  are in the type of localized block. In addition, strong compression regions are close to several regions of high expansion. This behavior is consistent with the physical intuitive that expansion regions can be identified just downstream of shock waves [49]. These random distributed shocklets and high expansion region lead to strong spatial gradient in flow fields, which pose much greater challenge for high-order schemes when implementing DNS for isotropic turbulence in supersonic regime. Numerically, few methods survive from such tough cases. The isotropic compressible turbulence with high turbulent Mach number

up to supersonic regime has been studied, which verifies that HGKS provides a valid tool for numerical and physical studies of compressible turbulence in supersonic regime. More challenging compressible turbulence problems will be investigated in the future, such as shock-boundary interaction and supersonic turbulent boundary layer.

#### 4. Conclusion

Based on the multi-scale physical transport and the coupled temporal-spatial gas evolution, the HGKS provides a useful tool for the numerical study of compressible turbulent flow. The performance of HGKS has been fully investigated for the DNS of isotropic compressible turbulence up to the supersonic regime. In order to increase the scale of computation, a parallel code of HGKS has been constructed with domain decomposition and MPI implementation. The resulting scheme is tested for Taylor-Green vortex problem, turbulent channel flow and isotropic compressible turbulence. It is the first successful DNS application of HGKS for turbulent flow from nearly incompressible to supersonic one. The scalability of parallel computation is validated, and the computational cost is comparable with the high-order finite difference method. For the nearly incompressible turbulent flow, the performance of HGKS is also comparable with the finite difference method. Based on the accuracy of the numerical solution, the numerical dissipation of the scheme in the turbulence simulation is quantitatively evaluated. As a mesoscopic method, the HGKS performs better than both LBM and DUGKS. More importantly, HGKS shows special advantages for the supersonic turbulence due to the accuracy and robustness. More challenging examples using HGKS at higher Reynolds numbers and different flow configurations will be investigated in the future.

#### Acknowledgement

This research is supported by National Natural Science Foundation of China (11701038, 11772281, 91852114), the Fundamental Research Funds for the Central Universities, and the National Numerical Windtunnel project. The authors would like to thank Prof. Xuesheng Chu for implementation of parallel computation, Prof. Lianping Wang for providing the channel turbulence data of LBM and DUGKS, and TianHe-II in Guangzhou for providing high performance computational resources.

#### References

- [1] H. Tennekes, J. L. Lumley, A first course in turbulence, MIT press (1972).
- [2] S.B. Pope. Turbulent flows, Cambridge, (2001).
- [3] J. Kim, P. Moin, R. Moser, Turbulence statistics in fully developed channel flow at low Reynolds number, J. Fluid. Mech. 177 (1987) 133-166.
- [4] M. Lee, R. Moser, Direct numerical simulation of turbulent channel flow up to  $Re_\tau \approx 5200$ , J. Fluid. Mech. 774 (2015) 395-415.
- [5] P. Moin, K. Mahesh, Direct numerical simulation: a tool in turbulence research, Annu. Rev. Fluid Mech. 30 (1998) 539-578.
- [6] L.P. Wang, S.Y. Chen, J.G. Brasseur, J.C. Wyngaard, Examination of hypotheses in the kolmogorov refined turbulence theory through high-resolution simulations. part 1. velocity field, J. Fluid Mech. 309 (1996) 113-156.

- [7] S.Y. Chen, G. D. Doolen, Lattice boltzmann method for fluid flows, *Annu. Rev. Fluid Mech.* 30 (1998) 329-364.
- [8] H.D. Yu, S.S. Girimaji, L.S. Luo, Lattice boltzmann simulations of decaying homogeneous isotropic turbulence, *Phys. Rev. E* 71 (2005) 016708.
- [9] G.Y. Cao, L. Pan, K. Xu, Three dimensional high-order gas-kinetic scheme for supersonic isotropic turbulence I: criterion for direct numerical simulation, *Computers & Fluids* 192 (2019) 104273.
- [10] S. Sarkar, G. Erlebacher, M.Y. Hussaini, H.O. Kreiss, The analysis and modelling of dilatational terms in compressible turbulence, *Journal of Fluid Mechanics*, 227 (1991) 473-493.
- [11] P. Sagaut, C. Cambon, *Homogeneous turbulence dynamics*, Springer (2008).
- [12] X.D. Liu, S. Osher, T. Chan, Weighted essentially non-oscillatory schemes, *J. Comput. Phys.* 115 (1994) 200-212.
- [13] G.S. Jiang, C.W. Shu, Efficient implementation of Weighted ENO schemes, *J. Comput. Phys.* 126 (1996) 202-228.
- [14] M. Castro, B. Costa, W. S. Don, High order weighted essentially non-oscillatory WENO-Z schemes for hyperbolic conservation laws, *J. Comput. Phys.* 230 (2011) 1766-1792.
- [15] S. K. Lele, Compact finite difference schemes with spectral-like resolution, *J. Comput. Phys.* 103 (1992) 16-42.
- [16] J.C. Wang, L.P. Wang, Z.L. Xiao, Y. Shi, S.Y. Chen, A hybrid numerical simulation of isotropic compressible turbulence, *J. Comput. Phys.* 229 (2010) 5257-5279.
- [17] S. Jeffrey, K. Abdollah, A. Juan, D. David, G. William, L. Elizabeth, M. Dimitri, *CFD vision 2030 study: a path to revolutionary computational aerosciences*, 2014.
- [18] P.L. Bhatnagar, E.P. Gross, M. Krook, A Model for Collision Processes in Gases I: Small Amplitude Processes in Charged and Neutral One-Component Systems, *Phys. Rev.* 94 (1954) 511-525.
- [19] S. Chapman, T.G. Cowling, *The Mathematical theory of Non-Uniform Gases*, third edition, Cambridge University Press, (1990).
- [20] K. Xu, Gas kinetic schemes for unsteady compressible flow simulations, *Lecture Note Ser.* 1998-03, Von Karman Institute for Fluid Dynamics Lecture (1998).
- [21] K. Xu, A gas-kinetic BGK scheme for the Navier-Stokes equations and its connection with artificial dissipation and Godunov method, *J. Comput. Phys.* 171 (2001) 289-335.
- [22] E.F. Toro, *Riemann Solvers and Numerical Methods for Fluid Dynamics*, Third Edition, Springer (2009).
- [23] J.Q. Li, Z.F. Du, A two-stage fourth order time-accurate discretization for Lax-Wendroff type flow solvers I. hyperbolic conservation laws, *SIAM J. Sci. Computing*, 38 (2016) 3046-3069.
- [24] J.Q. Li, Two-stage fourth order: temporal-spatial coupling in computational fluid dynamics (CFD), *Advances in Aerodynamics*, (2019) 1:3.
- [25] L. Pan, K. Xu, Q.B. Li, J.Q. Li, An efficient and accurate two-stage fourth-order gas-kinetic scheme for the Navier-Stokes equations, *J. Comput. Phys.* 326 (2016) 197-221.
- [26] L. Pan, K. Xu, Two-stage fourth-order gas-kinetic scheme for three-dimensional Euler and Navier-Stokes solutions, *Int. J. Comput. Fluid Dynamics*, 32 (2018) 395-411.
- [27] X. Ji, F.X. Zhao, W. Shyy, K. Xu, A family of high-order gas-kinetic schemes and its comparison with Riemann solver based high-order methods, *J. Comput. Phys.* 356 (2018) 150-173.
- [28] G.Y. Cao, H.L. Liu, K. Xu, Physical modeling and numerical studies of three-dimensional non-equilibrium multi-temperature flows, *Physics of Fluids* 30 (2018) 126104.
- [29] M. Righi, A gas-kinetic scheme for turbulent flow, *Turbul Combust* 97 (2016) 121-139.
- [30] S. Tan, Q.B. Li, Z.X. Xiao, S. Fu, Gas kinetic scheme for turbulence simulation. *Aerospace Science and Technology* 78 (2018) 214-27.
- [31] G.Y. Cao, H.M. Su, J.X. Xu, K. Xu, Implicit high-order gas kinetic scheme for turbulence simulation, *Aerospace Science and Technology* 92 (2019) 958-971.
- [32] M.P.I. Forum, *MPI: A Message-Passing Interface Standard, Version 2.2*. High Performance Computing Center Stuttgart (2009).
- [33] J. Debonis, Solutions of the Taylor-Green vortex problem using high-resolution explicit finite difference

- methods, AIAA 2013-0382.
- [34] Y.T. Bo, P. Wang, Z.L. Guo, L.P. Wang, DUGKS simulations of three-dimensional TaylorGreen vortex flow and turbulent channel flow, *Computers and Fluids* 155 (2017) 921.
  - [35] K. Xu, *Direct modeling for computational fluid dynamics: construction and application of unified gas kinetic schemes*, World Scientific (2015).
  - [36] M.E. Brachet, D.I. Meiron, S.A. Orszag, B.G. Nickel, R.H. Morf, U. Frisch, Small-scale structure of the Taylor-Green vortex, *J. Fluid. Mech.* 130 (1983) 411-452.
  - [37] M.A. Gallis, N.P. Bitter, T.P. Koehler, J.R. Torczynski, S.J. Plimpton, and G. Papadakis, Molecular-level simulations of turbulence and its decay, *Phys. Rev. L* 118 (2017) 064501.
  - [38] J. R. Bull, A. Jameson, Simulation of the compressible Taylor-Green vortex using high-order flux reconstruction schemes, AIAA 2014-3210.
  - [39] C. Bogey, C. Bailly, A family of low dispersive and low dissipative explicit schemes for flow and noise computations, *J. Comput. Phys.* 194 (2004) 194-214.
  - [40] J. Boris, F.F. Grinstein, E. Oran, R. Kolbe, New insights into large eddy simulation. *Fluid Dyn Res* 10 (1992) 199-228.
  - [41] A.W. Vreman, An eddy-viscosity subgrid-scale model for turbulent shear flow: Algebraic theory and applications, *Physics of Fluids*, 16 (2004) 3670-3681.
  - [42] S. Hoyas, J. Jiménez, Scaling of the velocity fluctuations in turbulent channels up to  $Re_\tau = 2003$ , *Physics of Fluids*, 18 (2006) 011702.
  - [43] R.B. Dean, Reynolds number dependence of skin friction and other bulk flow variables in two-dimensional rectangular duct flow, *Trans, ASME I: J. Fluids Engng* (1978).
  - [44] D.C. Wilcox, *Turbulence modeling for CFD*, DCW industries La Canada, CA (1998).
  - [45] R. Samtaney, D.I. Pullin, B. Kosović, Direct numerical simulation of decaying compressible turbulence and shocklet statistics, *Physics of Fluids* 13 (2001) 1415-1430.
  - [46] T. Passot, A. Pouquet, Numerical simulation of compressible homogeneous flows in the turbulent regime, *J. Fluid Mech.* 181 (1987) 441-466.
  - [47] A. Yoshizawa, K. Horiuti, A statistically-derived subgrid-scale kinetic energy model for the large-eddy simulation of turbulent flows, *Journal of the Physical Society of Japan*, 54 (1985) 2834-2839.
  - [48] J.C. Wang, M.P. Wan, S. Chen, S.Y. Chen, Kinetic energy transfer in compressible isotropic turbulence, *Journal of Fluid Mechanics*, 841 (2018) 581-613.
  - [49] J.C. Wang, M.P. Wan, S. Chen, C.Y. Xie, S.Y. Chen, Effect of shock waves on the statistics and scaling in compressible isotropic turbulence, *Phys. Rev. E* 97 (2018) 043108.